

# A Multi-Fidelity Emulator for the Matter Power Spectrum using Gaussian Processes

Ming-Feng Ho,<sup>1\*</sup> Simeon Bird,<sup>1†</sup> Christian R. Shelton.<sup>2</sup>

<sup>1</sup>*Department of Physics & Astronomy, University of California, Riverside, 900 University Ave., Riverside, CA 92521, USA*

<sup>2</sup>*Department of Computer Science & Engineering, University of California, Riverside, 900 University Ave., Riverside, CA 92521, USA*

5 May 2021

## ABSTRACT

We present methods for emulating the matter power spectrum which effectively combine information from cosmological  $N$ -body simulations at different resolutions. An emulator allows estimation of simulation output by interpolating across the parameter space of a handful of simulations. We present the first implementation of multi-fidelity emulation in cosmology, where many low-resolution simulations are combined with a few high-resolution simulations to achieve an increased emulation accuracy. The power spectrum’s dependence on cosmology is learned from the low-resolution simulations, which are in turn calibrated using high-resolution simulations. We show that our multi-fidelity emulator can achieve percent-level accuracy on average with only 3 high-fidelity simulations and outperforms a single-fidelity emulator that uses 11 simulations. With a fixed number of high-fidelity training simulations, we show that our multi-fidelity emulator is  $\simeq 100$  times better than a single-fidelity emulator at  $k \leq 2 h\text{Mpc}^{-1}$ , and  $\simeq 20$  times better at  $3 \leq k < 6.4 h\text{Mpc}^{-1}$ . Multi-fidelity emulation is fast to train, using only a simple modification to standard Gaussian processes. Our proposed emulator shows a new way to predict non-linear scales by fusing simulations from different fidelities.

**Key words:** cosmology: theory - cosmology: numerical - methods: statistical

## 1 INTRODUCTION

Next generation large scale structure surveys, such as DES<sup>1</sup> (Abbott et al. 2020), LSST (Rubin Observatory)<sup>2</sup> (Tyson 2002), EUCLID<sup>3</sup> (Amendola et al. 2018), DESI<sup>4</sup> (DESI Collaboration et al. 2016), and the Roman Space Telescope (WFIRST) (Spergel et al. 2013) will probe gravitational clustering and galaxy formation at small scales with high accuracy. Thus, the future of cosmology relies on exploiting the information in non-linear structure formation at small scales, where numerical  $N$ -body simulations must be used to give accurate theoretical predictions.

Cosmological linear perturbation theory provides accurate analytic predictions on the clustering of mass up to  $k \sim 0.1 h\text{Mpc}^{-1}$ . Despite the standard model’s success, several fundamental physics puzzles are still unanswered: the accelerated expansion of the Universe (Caldwell

& Kamionkowski 2009), the nature of dark matter (Feng 2010), and the sum of the neutrino masses (Wong 2011). To answer these questions and constrain the cosmological parameters using future surveys, theoretical predictions from numerical simulations must be accurate on smaller scales. As a primary summary statistic, the matter power spectrum needs to be at percent-level precision from linear scales up to  $k \sim 10 h\text{Mpc}^{-1}$  (Schneider et al. 2016).

Modelling non-linear gravitational clustering is done using  $N$ -body simulations, where a dark matter fluid is sampled by macro-particles and evolved using a smoothed gravitational force. Each macro-particle is representative of an ensemble of microscopic dark matter particles. Generations of computational physicists have improved the accuracy of the gravitational evolution, and driven the mass resolution of the simulations ever higher with quicker and more scalable algorithms (Hockney & Eastwood 1988; Barnes & Hut 1986; Couchman et al. 1995; Greengard & Rokhlin 1987; Dehnen 2002).

The mass resolution, proportional to the number of simulation particles, pushes the computational limits of contemporary supercomputers. Though high-fidelity simulations with the finest mass resolution make robust theoretical pre-

\* E-mail: mho026@ucr.edu

† E-mail: sbird@ucr.edu

<sup>1</sup> <https://www.darkenergysurvey.org>

<sup>2</sup> <https://www.lsst.org>

<sup>3</sup> <https://sci.esa.int/web/euclid>

<sup>4</sup> <https://www.desi.lbl.gov>

dictions on non-linear scales, they are costly to obtain. It will be a challenge to infer cosmological parameters from non-linear scales using only high-fidelity numerical simulations. Currently, studies require as many high-fidelity simulations as possible to explore alternative cosmologies and galaxy formation scenarios. To adequately sample a high-dimensional input parameter space with MCMC, millions of samples are needed, while only tens of high-fidelity simulations are computationally available by contemporary supercomputers.

An effective way to perform accurate cosmological inference with a handful of simulations is to use *emulators*. Emulators are flexible statistical models, usually built with Gaussian processes, which learn the mapping from input cosmological parameters to summary statistics. This reduces the number of costly forward simulations by effectively interpolating the function outputs.

Most cosmological emulators implement a Latin hypercube strategy to sample the high-dimensional parameter space (5 dimensions for  $\Lambda$ CDM; 8 dimensions including neutrino mass and dynamical dark energy). Latin hypercube sampling, proposed by Heitmann et al. (2009) for cosmological applications, is a uniform deterministic sampling scheme that avoids samples overlapping in any projected dimension and prevents samples clustered in the subspace. Although Latin hypercube sampling reduces the required number of training simulations, it still requires 37 training points for a percent level accurate emulator with 5 parameters in Heitmann et al. (2009). Performing 37 high-resolution simulations requires large supercomputer resources.

Here we propose improving the process of building cosmological emulators from simulations with multi-fidelity models. Multi-fidelity models (Kennedy & O’Hagan 2000) minimize the computational cost by combining the predictive power of simulations at different resolutions. They fuse the expensive but accurate *high fidelity* data with cheaply-obtained *low fidelity* approximations. One standard model used by the multi-fidelity emulation is a *multi-output Gaussian process* (Bonilla et al. 2008). A multi-output Gaussian process (multi-output GP) generalizes a single-output GP to multiple outputs, while building a cross-covariance function to model the shared information between outputs. In this paper, low and high fidelity correspond to simulations at different resolutions. High-fidelity simulations have a finer mass resolution while low-fidelity simulations have a coarser mass resolution.

We present a multi-fidelity emulator for the matter power spectrum, as output by the cosmological simulation code MP-GADGET (Springel & Hernquist 2003; Feng et al. 2018a). In this paper we perform simulations in relatively small boxes to check the validity of our techniques. In future work we will run large simulations and build a multi-fidelity emulator converged in a specific scale and redshift range, ready for applying to observations.

We use Latin hypercube sampling with small simulations in a 256 Mpc/h box: a fast but low resolution version with  $128^3$  dark-matter particles and a slow but high resolution version with  $512^3$  particles. Even with only 3 high-fidelity simulations and 50 low-fidelity simulations, we show that we can predict the high-resolution matter power spectrum at percent-level accuracy on average at  $k \leq 6.4 h\text{Mpc}^{-1}$  at  $z = 0$ , with a total computational cost  $\lesssim 4$  high-fidelity simulations. Although we only show our

application to the matter power spectrum, the methods presented in this paper could apply to other summary statistics, e.g., the halo mass function or the Lyman- $\alpha$  1D flux power spectrum.

van Daalen et al. (2011) showed that a dark matter only simulation is worse than 1% accurate at  $k > 0.1 h\text{Mpc}^{-1}$  without AGN feedback. Furthermore, baryon cooling can alter the power spectrum at  $k \sim 10 h\text{Mpc}^{-1}$  (White 2004). Although the multi-fidelity emulator proposed in this paper is for dark matter only simulations, in future, we will extend the framework to treat a more complex simulation with baryons or AGN feedback as the high-fidelity case. Here we will validate that a multi-fidelity emulator is useful in the simplest case of  $N$ -body simulations, leaving building an emulator for hydrodynamical simulations to future work.

We build two types of multi-fidelity emulators. One uses the linear autoregressive model of Kennedy & O’Hagan (2000) (first-order autoregressive model, AR1), which we will call the “linear multi-fidelity model.” The second multi-fidelity emulator uses the non-linear fusion model of Perdikaris et al. (2017) (nonlinear auto-regressive Gaussian process, NARGP), and which we call the “non-linear multi-fidelity emulator.”<sup>5</sup> Kennedy & O’Hagan (2000) model the scaling factor between fidelities as a scalar, while Perdikaris et al. (2017) allow the scaling factor to depend on input parameters. Instead of modelling all  $k$  outputs as one GP, we emulate each  $k$  output of the power spectrum  $P(k)$  separately using a single-output multi-fidelity emulator.<sup>6</sup> Our implementation of AR1 and NARGP is based on `emukit` (Paleyes et al. 2019),<sup>7</sup> an open-source package for emulation and decision making under uncertainty, with the modifications mentioned above.<sup>8</sup> Our code for multi-fidelity emulation in the matter power spectrum is publicly available at [https://github.com/jibanCat/matter\\_multi\\_fidelity\\_emu](https://github.com/jibanCat/matter_multi_fidelity_emu).

To train the multi-fidelity emulator using as few high-resolution simulations as possible, we also propose a method for selecting high-fidelity training samples, based on minimizing the loss computed among the low-fidelity simulations. By optimizing the low-fidelity emulator’s loss, we show that one can efficiently train a multi-fidelity emulator by avoiding worst-case combinations of the high-fidelity training samples.

Emulators have been applied extensively in the field of cosmological inference. Heitmann et al. (2006); Habib et al. (2007) proposed a cosmic calibration project to make percent-level predictions on the matter power spectrum using a Bayesian emulator. Heitmann et al. (2009); Lawrence et al. (2010); Heitmann et al. (2014) implemented this cosmic emulator in their Coyote Universe suite using 37 high-resolution simulations. Heitmann et al. (2016); Lawrence

<sup>5</sup> AR1 and NARGP are acronyms used in Perdikaris et al. (2017); Cutajar et al. (2019). In this paper, AR1 and linear multi-fidelity emulator are interchangeable, and NARGP and non-linear multi-fidelity emulator are interchangeable.

<sup>6</sup> Takhtaganov et al. (2019) refers to this approach as the many single-output approach (MS).

<sup>7</sup> <https://github.com/EmuKit/emukit>

<sup>8</sup> For a detailed comparison between AR1 and NARGP, see Cutajar et al. (2019). An example code for the comparison between AR1 and NARGP can be found in Emukit’s examples.

et al. (2017) designed the Mira-Titan Universe suite to train emulators to make precise theoretical predictions using 36 simulations. The latest Euclid preparation (Euclid Collaboration et al. 2020) runs 250 simulations ( $3000^3$  particles) to prepare their emulator for the matter power spectrum. Besides Gaussian processes, Agarwal et al. (2014) used a neural network to build a cosmic emulator from 6380  $N$ -body simulations spanning 580 cosmologies.

Beyond the matter power spectrum, emulators have been trained to predict the halo mass function (Bocquet et al. 2020), the concentration-mass relation for dark-matter haloes (Kwan et al. 2013), the galaxy power spectrum (Kwan et al. 2015), the galaxy correlation function (Zhai et al. 2019), the halo bias (McClintock et al. 2019), weak lensing peak counts (Liu et al. 2015), the cosmic shear covariance (Harnois-Déraps et al. 2019), weak lensing voids (Davies et al. 2020), the 21 cm signal (Kern et al. 2017), and the Lyman- $\alpha$  1D flux power spectrum (Bird et al. 2019). They also have been used for inferring beyond- $\Lambda$ CDM cosmologies (Giblin et al. 2019; Pedersen et al. 2020) and  $f(R)$  gravity cosmologies (Ramachandra et al. 2020). While all these models successfully emulate forward simulations using high-fidelity simulations, one question which remains is how to minimize the number of necessary high-fidelity simulations to achieve a given accuracy.

Rogers et al. (2019) proposed using Bayesian optimization to improve emulator accuracy by a sequential choice of new simulation points designed to globally optimize the emulator function. Similar approaches to iterative selection of training data in a cosmological parameter space have been presented by Takhtaganov et al. (2019); Pellejero-Ibañez et al. (2020). Computer scientists and engineers, including Huang et al. (2006); Forrester et al. (2007); Lam et al. (2015); Poloczek et al. (2016); McLeod et al. (2017), have extensively studied combining multi-fidelity methods with Bayesian optimization.<sup>9</sup> Multi-fidelity Bayesian optimization arises when a cheaper approximation to the object function exists.

Computational astrophysicists have used methods similar to multi-fidelity modelling to minimize the cost of performing high-resolution simulations (Lukić et al. 2015; Chartier et al. 2020). A notable example is Richardson extrapolation (Richardson 1911), a numerical method to improve a simulation’s accuracy by combining a sequence of simulations with varied spatial resolutions (but fixed cosmologies).

Recent developments in generative adversarial networks (GAN) have also enabled super-resolution applications in cosmology. Kodi Ramanah et al. (2020) used a generative adversarial network (GAN) to map the low-resolution density fields to high-resolution. Li et al. (2020) used a super-resolution GAN to map the particle displacements from low-resolution  $N$ -body simulations to their high-resolution counterparts. This allows large volume simulations at low resolution to be combined with small volume but higher resolution simulations to create a single (artificial) large volume simulation at high resolution. In principle, super-resolution simulations could be implemented as a multi-fidelity emula-

**Table 1.** Notations and definitions

| Notation              | Description   |
|-----------------------|---|
| HR                    | High-resolution simulation, $512^3$ particles                             |
| LR                    | Low-resolution simulation, $128^3$ particles                              |
| $x_{i,t}$             | Input cosmological parameters at $i$ th simulation at fidelity $t$        |
| $y_{i,t}$             | Matter power spectrum at $i$ th simulation at fidelity $t$ , at log scale |
| $n_t$                 | Number of simulations at fidelity $t$                                     |
| $N_{\text{ptl,side}}$ | Number of particles per box side  |

tor’s high-fidelity training set, constraining cosmology without running any costly high fidelity simulations.

In Section 2, we briefly describe the simulation code, MP-GADGET, for training the emulator. We recap the general formalism of a single-fidelity Gaussian process emulator in Section 3. Section 4 describes the formalism of a multi-fidelity emulator (MFEmulator). We explain our sampling strategy in Section 5. Section 6 shows the results, with comparisons between multi-fidelity emulation and single-fidelity emulation. We summarize the runtime for the MP-GADGET simulations in Section 7. We conclude with a summary of key contributions and potential applications of our work in Section 8.

## 2 SIMULATIONS

We prepare our training set by running dark matter only simulations using the massively parallel  $N$ -body code MP-GADGET (Feng et al. 2018b).<sup>10</sup> MP-GADGET is a publicly available  $N$ -body+Hydro cosmological simulation code derived from GADGET3 (Springel & Hernquist 2003). It has successfully performed a hydrodynamical simulation using all 8032 *Frontera* nodes, a total of 449792 cores, demonstrating its good scalability properties. The gravitational forces are computed using a Fourier transform based particle-mesh algorithm on large scales and a Barnes-Hut tree on small scales.

MP-GADGET simulations are initialized from the linear power spectrum produced by CLASS (Lesgourgues 2011) at  $z = 99$  using the Zel’dovich approximation (Zel’dovich 1970). The dark matter particles then evolve through gravitational dynamics. The matter power spectra are computed from the output snapshots of MP-GADGET, and used as our emulation targets.

The matter power spectrum,  $P(k)$ , is a compressed summary statistic of the over-density field,  $\delta(x)$ , evaluated as an angle average of the Fourier-transformed overdensity field:

$$P(|\mathbf{k}|) = \langle \hat{\delta}^*(k) \hat{\delta}(k) \rangle, \quad (1)$$

$$\hat{\delta}(\mathbf{k}) = \int d^3\mathbf{r} \delta(\mathbf{r}) e^{-2\pi i \mathbf{k} \cdot \mathbf{r}}, \quad (2)$$

For a multi-fidelity problem, our data are from simulations at different resolutions. Since low resolution simulations are cheaper to obtain (but are only approximations to the high resolution results), we typically have a handful of high-fidelity data and many low-fidelity approximations.

<sup>9</sup> Frazier (2018) has a subsection that provides a short review on multi-fidelity Bayesian optimization.

<sup>10</sup> <https://github.com/MP-Gadget/MP-Gadget/>

To make the text of this section consistent with the following sections, we provide some notation to bridge the terminology, summarized in Table 1. We have data from  $s$  different fidelities (simulation resolutions). For each fidelity, we have pairs of inputs and outputs  $\mathcal{D}_t = \{x_{i,t}, y_{i,t}\} = \{\mathbf{x}_t, \mathbf{y}_t\}$ , where  $t = 1, \dots, s$  denotes the fidelity level from low to high, and  $i = 1, \dots, n_t$  where  $n_t$  is the number of data pairs at fidelity  $t$  and  $i$  indexes each individual simulation. The data pairs  $\mathcal{D}_t = \{\mathbf{x}_t, \mathbf{y}_t\}$  for our emulation setup are the cosmological parameters of the simulations and the power spectrum outputs.

For our simulation setup, we have  $s = 2$  for two mass resolutions:  $128^3$  and  $512^3$  dark matter only simulations. We will denote  $128^3$  as low-resolution (LR,  $t = 1$ ) and  $512^3$  as high-resolution (HR,  $t = 2$ ) simulations.

Each fidelity will have a different number of simulations,  $n_t$ . The principle is to have the number of LR simulations much larger than the number of HR simulations,  $n_1 > n_2$ . The compute time for LR ( $N_{\text{ptl,side}} = 128$ ) is  $\sim 20$  core hours and  $\sim 2000$  core hours for HR ( $N_{\text{ptl,side}} = 512$ ). We will empirically show we only need 3 HR and 50 LR to train a multi-fidelity emulator with an average emulator error per  $k$  smaller than 1%.

We do not emulate the matter power spectrum across redshifts, conditioning on a given redshift bin  $z_0$ . We generally focus on  $z_0 = 0$ , but will discuss multi-fidelity emulators at  $z_0 = 1$  and  $z_0 = 2$  in Section 6.4.2.

## 2.1 Preprocessing treatments to the power spectrum from MP-Gadget

A numerical simulation is constrained by its box size and number of particles. The mass resolution limits the smallest scale (the highest  $k$ ) of the power spectrum. Thus, high-fidelity simulations can model smaller scales, not fully resolved in low-fidelity simulations, as shown in Figure 1.

For  $k$  larger than the mean particle spacing,  $P(k)$  is substantially larger than the resolved value, due to artifacts of the macro-particle sampling. The scale of the mean particle spacing is

$$k_{\text{spacing}} = 2\pi \frac{N_{\text{ptl,side}}}{L_{\text{box}}}, \quad (3)$$

where  $N_{\text{ptl,side}}$  is the number of particles per side of the box. For instance, if we have  $512^3$  particles in the box, then  $N_{\text{ptl,side}} = 512$ . The  $L_{\text{box}}$  is the size of the simulation box in units of Mpc/h.

We use the same set of matter power spectrum  $k$  bins for all fidelities. The available information at small scales is sparse for the low-fidelity spectrum. To resolve the issue, we fix the  $k$  bins to high fidelity and linearly interpolate the low-fidelity power spectrum in a  $\log_{10}$  scale ( $\log_{10} P(k)$ ) onto the high-fidelity  $k$  bins. The maximum  $k$  is set to be  $\simeq 6.4 h \text{Mpc}^{-1}$  when using  $N_{\text{ptl,side}} = 128$  as our low-fidelity training set. However, in practice we found that  $128^3$  and  $512^3$  simulations shared similar  $k$  bins with small offsets at small scales.

We do not model the high-fidelity spectrum with  $k$  larger than the maximum  $k$  of the low-fidelity spectrum:

$$\max k_{t=2} = \max k_{t=1}, \quad (4)$$

where  $t$  indicates the fidelity level and  $t = 2$  is the highest

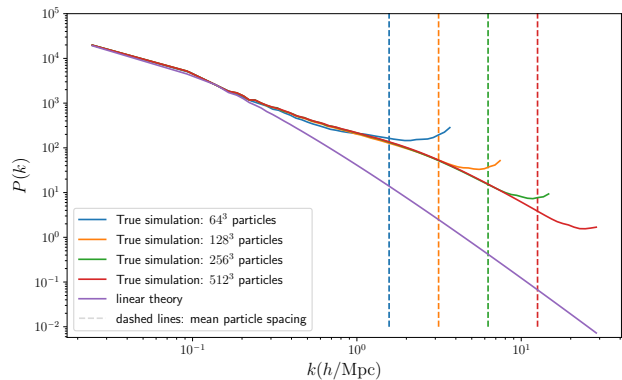


**Figure 1.** The matter power spectrum output by MP-GADGET with different mass resolutions. The vertical dash lines indicated the mean particle spacing  $k_{\text{spacing}}$  for a given mass resolution. **(Blue):** The matter power spectrum from a dark-matter only MP-GADGET simulation with  $64^3$  particles. **(Orange):** The matter power spectrum from MP-GADGET with  $128^3$  particles. **(Green):** The matter power spectrum from MP-GADGET with  $256^3$  particles. **(Red):** The matter power spectrum from MP-GADGET with  $512^3$  particles. **(Purple):** Linear theory power spectrum. The cosmology parameters are  $h = 0.675$ ,  $\Omega_0 = 0.278$ ,  $\Omega_b = 0.0474$ ,  $A_s = 1.695 \cdot 10^{-1}$ ,  $n_s = 9.405 \cdot 10^{-1}$ .

fidelity. If we do not have any data at a given  $k$  from low-fidelity, we cannot extract the correlations between fidelities without other more significant assumptions. In other words, the maximum  $k$  we can model is limited by the data available from the low-fidelity simulations, which always have a lower maximum  $k$  than high-fidelity simulations. We note that it is possible to get a higher maximum  $k$  by increasing the size of the PM grid size used for estimating the power spectrum, although we do not do that here.

We do model the low-fidelity  $P(k)$  even on scales smaller than the mean particle spacing,  $k > k_{\text{spacing}}$ . We made this particular decision because we have a prior belief that even though  $P(k > k_{\text{spacing}})$  is highly biased, it still captures some information about how  $P(k)$  depends on cosmological parameters. Thus, we should be able to exploit the correlations between fidelities and improve the emulator accuracy at those scales.

We summarize the pre-processing decisions we made in this work:

- (i) Use the same set of  $k$  bins across different fidelities.
- (ii) Preserve all available  $P(k)$  from low-fidelity, even scales smaller than the simulation's mean particle spacing.

## 3 SINGLE-FIDELITY EMULATOR

Here we briefly recap how we train a single-fidelity emulator. Readers familiar with this material may wish to skip to Section 4. The notation we use in this section follows those of Perdikaris et al. (2017); Cutajar et al. (2019). Consider a supervised learning problem, in which we wish to learn the mapping relation,  $f$ , between a set of input and output pairs  $\mathcal{D} = \{x_i, y_i\} = \{\mathbf{x}, \mathbf{y}\}$ , where  $i = 1, \dots, n$ :

$$\mathbf{y} = f(\mathbf{x}), \quad \text{with } \mathbf{x} \in \mathbb{R}^d, \quad (5)$$

where  $d$  is the dimension of the input space. A Gaussian process (GP) (Rasmussen & Williams 2005) is a probabilistic framework modelling the observations,  $\mathbf{y}$ , as draws from a noisy realization of a single random function  $f$  with a likelihood  $p(\mathbf{y} | f)$ . It models the distribution over  $f$

$$p(f) = \mathcal{GP}(f; \mu, K), \quad (6)$$

with  $\mu$  the GP mean prior function, which is usually assumed to be a zero mean prior, and  $K$  the covariance kernel function specified by a vector of hyperparameters,  $\boldsymbol{\theta}$ . For a given set of inputs,  $x_1, x_2, \dots, x_n$ , the kernel function evaluated on these points produces a symmetric, positive-definite covariance matrix  $K_{ij} = K(x_i, x_j; \boldsymbol{\theta})$  with  $K \in \mathbb{R}^{n \times n}$ .

The choice of the covariance kernel depends on our prior knowledge about the data. The hyperparameters of a chosen kernel are optimized by maximizing the marginal log-likelihood:

$$\log p(\mathbf{y} | \mathbf{x}, \boldsymbol{\theta}) = -\frac{1}{2} \log |\mathbf{K}| - \frac{1}{2} \mathbf{y}^\top \mathbf{K}^{-1} \mathbf{y} - \frac{n}{2} \log 2\pi. \quad (7)$$

For an emulator, the main purpose is to predict an output  $f_* = f(x_*)$  from a new input point  $x_*$ , given the provided data  $\mathcal{D}$ .

$$\begin{aligned} p(f_* | \mathcal{D}, x_*) &= \mathcal{N}(f_* | \mu_*(x_*), \sigma_*^2(x_*)), \\ \mu_*(x_*) &= \mathbf{k}_{*n} \mathbf{K}^{-1} \mathbf{y}, \\ \sigma_*^2(x_*) &= K(x_*, x_*) - \mathbf{k}_{*n} \mathbf{K}^{-1} \mathbf{k}_{*n}^\top, \end{aligned} \quad (8)$$

where  $\mu_*$  is the posterior mean and  $\sigma_*$  is the standard deviation of the uncertainty in the estimate of the predictions. The vector  $\mathbf{k}_{*n}$  is the covariance between the new point and trained data,  $\mathbf{k}_{*n} = [K(x_*, x_1), \dots, K(x_*, x_n)]$ .

### 3.1 Gaussian process emulator

Here we briefly describe how a GP connects to an emulator. Consider we have a set of dark matter only simulations with fixed box size and mass resolution. At each redshift bin  $z_0$ , we can compute the matter power spectrum,  $P(k, z = z_0)$ , given a set of input parameters. We will use the log power spectrum,  $\log_{10} P(k, z = z_0)$ , as our training data.

Input parameters are chosen depending on the science goals of the experiment. Here we choose to vary the  $\Lambda$ CDM cosmology parameters  $\{h, \Omega_0, \Omega_b, A_s, n_s\}$ , which are the Hubble parameter  $h = H_0 / (100 \text{ km s}^{-1} \text{ Mpc}^{-1})$ , the total matter density  $\Omega_0$ , the baryon density  $\Omega_b$ , primordial amplitude of scalar fluctuations  $A_s$ , and the scalar spectral index  $n_s$ .

The training data,  $\mathcal{D} = \{x_i, y_i\}$  thus are defined as

$$\begin{aligned} x_i &= [h_i, \Omega_{0i}, \Omega_{bi}, A_{si}, n_{si}]; \\ y_i &= \log_{10} P(k, z = z_0), \end{aligned}$$

where  $i = 1, \dots, n$  indicates the  $i$ th simulation we run with this specific set of input parameters. For a single simulation, the matter power spectrum  $P(k, z = z_0)$  will be binned into several  $k$  modes. Each input parameter set  $\{h, \Omega_0, \Omega_b, A_s, n_s\}$  will generate multiple outputs corresponding to different  $k$  modes.

As we will mention in Section 4.2, we model each  $k$  mode output with a different GP to allow the hyperparameters to depend on  $k$ . To make a fair comparison with MFEmulator, we also model the single-fidelity emulator as many single-output GPs, implying kernel parameters are independent at

each mode. However, we have empirically verified that this single-fidelity emulator's performance is similar to the emulator using a GP with shared kernel parameters across all  $k$  modes.

The rest of the modelling is choosing an appropriate covariance function  $K(x, x')$ . We use a squared exponential kernel and use automatic relevance determination (ARD) weights for each input dimension. ARD assigns each input dimension,  $x_i$ , a separate hyperparameter,  $w_i$ :

$$K(x, x'; \boldsymbol{\theta}) = \sigma^2 \exp\left(-\frac{1}{2} \sum_{i=1}^d w_i (x_i - x'_i)^2\right) \quad (9)$$

where  $i = 1, \dots, d$  indicates the dimension of the input space  $x \in \mathbb{R}^d$ . We note that we assign independent hyperparameters,  $\boldsymbol{\theta} = \{\sigma^2, w_1, \dots, w_d\}$ , for each  $k$  mode.  $\sigma^2$  is the variance parameter for the squared exponential kernel,  $\{w_i\}_{i=1}^d$  are the ARD weights.  $\{w_i\}_{i=1}^d$  are inverse length scales, which define the degree of smoothness at a given input dimension. A larger  $w_i$  corresponds to a smaller length scale, reflecting that the learned function varies more in the  $i$ th dimension. On the other hand, a smaller  $w_i$  implies a larger length scale, indicating that the learned function is smoother along the  $i$ th dimension. ARD allows each dimension of the learned function to have a different degree of smoothness.

We do not decompose the power spectrum into principle components for training the emulators, as described by Heitmann et al. (2006); Habib et al. (2007) because we want to compare single-fidelity emulators to the multi-fidelity emulators, and an MFEmulator only has a limited number of high-resolution simulations available. In our default case, we only have 3 high-resolution simulations for an MFEmulator, and it is not sensible to perform dimension reduction on these three power spectra.

### 3.2 Latin hypercube sampling

Since we use a squared exponential kernel to train our GP, uniformly spreading out sampling points will be preferred to minimize the worst case interpolation error. As Heitmann et al. (2009) mentioned, a space-filling Latin hypercube design is well suited for GP model emulators.

For a training set with  $d$ -dimensional inputs and  $N$  simulations, an  $N^d$  grid is created first. The Latin hypercube design is better than a grid since no projected points will overlap in any dimension. Also, it is better than random uniform sampling because the chosen points will not crowd together in any subspace.

We apply a Latin hypercube design on the input parameter space,  $\{h, \Omega_0, \Omega_b, A_s, n_s\}$ . The priors for input parameters are bounded uniform priors:

$$\begin{aligned} h &\sim \mathcal{U}[0.65, 0.75]; \\ \Omega_0 &\sim \mathcal{U}[0.268, 0.308]; \\ A_s &\sim \mathcal{U}[1.5 \times 10^{-9}, 2.8 \times 10^{-9}]; \\ n_s &\sim \mathcal{U}[0.9, 0.99]; \\ \Omega_b &\sim \mathcal{U}[0.0452, 0.492]. \end{aligned} \quad (10)$$

The total density of dark energy is restricted to be  $\Omega_\Lambda = 1 - \Omega_0$ . The code to handle the simulation input files and Latin hypercube design is publicly available at <https://github.com/jibanCat/SimulationRunnerDM>.

#### 4 MULTI-FIDELITY EMULATOR

In this section, we describe how we train a multi-fidelity emulator. We outline the modelling assumptions in Section 4.1. Section 4.2 describes the formalism of the linear multi-fidelity emulator proposed by Kennedy & O’Hagan (2000), a multi-output GP with a linear correlation between fidelities. Section 4.3 outlines the non-linear multi-fidelity emulator of Perdikaris et al. (2017), which models the correlation between fidelities as a function of cosmological parameters. We follow the notation and formalism of Kennedy & O’Hagan (2000); Perdikaris et al. (2017); Cutajar et al. (2019).

##### 4.1 General assumptions

Here we outline our modelling assumptions, following the assumptions made in Kennedy & O’Hagan (2000):

(i) **Correlations between the code fidelities:** For an  $N$ -body simulation, the simulation cost depends on the mass resolution. We assume a simulation with a low mass resolution can approximate a simulation with a high mass resolution. The matter power spectrum from different fidelities is strongly correlated at large scales since all fidelities are resolved and the mass resolution has negligible effects. At small scales, however, we expect different fidelities are only weakly correlated.

(ii) **Smoothness:** For an emulation problem, we assume that neighbouring inputs give similar outputs. For example, suppose two sets of input parameters to MP-GADGET are close to each other. In that case, we assume that an  $N$ -body simulation will provide a similar outcome.

(iii) **The prior belief on each fidelity is a Gaussian process:** We assume a prior belief that the mapping from code input to output is a Gaussian process for each fidelity.

The first assumption is the core assumption of a multi-fidelity emulator. Different levels of the same code are simulating the same physical reality. It is thus reasonable to assume different code fidelities should correlate at some level. However, a naive simulation, for example,  $N_{\text{ptl,side}} = 16$  could only barely approximate a HR with  $N_{\text{ptl,side}} = 512$ . Therefore, we should also assume the correlation between fidelities depends on the distance between two fidelities in the dimension of mass resolution.

There is thus a trade-off between the strength of correlation and the computational expense: for example, a simulation with  $N_{\text{ptl,side}} = 256$  provides more information about a HR ( $N_{\text{ptl,side}} = 512$ ), but running a  $256^3$  simulation is only 8 times cheaper than running a HR.

One can select an optimal choice of simulation cost by balancing the computational time and the emulation accuracy. Here we choose  $N_{\text{ptl,side}} = 128$  for our low-fidelity simulations because:

(i) The maximum  $k$  is  $\simeq 6.4 h\text{Mpc}^{-1}$ , which includes enough non-linear scales to test the emulation accuracy;

(ii) A  $128^3$  simulation is 64 times cheaper than a HR, and thus the resolution difference between  $N_{\text{ptl,side}} = 128$  and  $N_{\text{ptl,side}} = 512$  is large enough to demonstrate whether simulations with lower costs can accelerate the training of an emulator.

In Section 6.4.1, we will show our method is applicable to simulations with different resolutions,  $N_{\text{ptl,side}} = 64$  and 256. Empirically, we found that using  $N_{\text{ptl,side}} = 256$  as low-fidelity works similar to  $N_{\text{ptl,side}} = 128$ , while  $N_{\text{ptl,side}} = 64$  gives a worse emulation accuracy.

The second assumption, the smoothness assumption, is the general assumption of a GP emulator. A GP emulator will have poor accuracy if the code does not behave similarly with similar input. The smoothness assumption is also the assumption behind the Latin hypercube sampling scheme (for a detailed discussion, see Heitmann et al. 2009).

A multi-fidelity emulation could in principle be implemented using other models (see Peherstorfer et al. (2018) for different data-fit models for surrogates). We chose to use GPs simply because their Bayesian approach supports uncertainty quantification and there is a well-developed community around GP emulation.

##### 4.2 Linear multi-fidelity emulator (AR1)

We have multi-fidelity data  $\mathcal{D}_t$  as described in Section 2. The final goal of a multi-fidelity emulator is to find a mapping relation  $f$  such that, from an arbitrary input vector  $x_*$ , we can always find the highest fidelity code output:

$$y_{s,*} = f(x_*). \quad (11)$$

As described by Kennedy & O’Hagan (2000), a linear autoregressive model can be applied in a multi-fidelity setting by assuming a hierarchical order between fidelities:

$$f_t(x) = \rho_t f_{t-1}(x) + \delta_t(x), \quad (12)$$

where  $f_t$  is the function emulated by a GP at  $t$  fidelity and  $f_{t-1}$  is the function emulated at the previous fidelity level ( $t - 1$ ).  $\rho_t$  is a constant scaling factor that describes the correlation between the function outputs  $y_t$  and  $y_{t-1}$ . The linear component of Eq 12 is  $\rho_t$ , which models the correlation between fidelities as a linear relation.  $\delta_t$  is a GP modelling the bias term:

$$\delta_t \sim \mathcal{GP}(\mu_{\delta_t}, K_t). \quad (13)$$

A multi-fidelity emulator is essentially inferencing the highest fidelity model conditioned on data from all model fidelities.

We modify Eq 12 so inference is performed on each  $k$  bin independently. For  $k = k_j$ , we have a multi-fidelity GP:

$$f_t(k = k_j, x) = \rho_t(k = k_j) (f_{t-1}(x, k = k_j) - \mu_{t-1}(k = k_j)) + \delta_t(x, k = k_j),$$

where we have independent kernel and scaling parameters for each  $k = k_j$  mode. For simplicity, we will drop the  $k = k_j$  notation in the rest of the paper:

$$f_t(x) = \rho_t(f_{t-1}(x) - \mu_{t-1}) + \delta_t(x). \quad (14)$$

The mean of the bias term,  $\mu_{\delta_t}$ , is assumed to be the zero mean function here.

For the low-fidelity part, we subtract the sample mean of the logarithm training power spectra,  $\log_{10} P(k)$ , and model the low fidelity part of the power spectra as a zero mean GP:

$$(f_1(x) - \mu_1) \sim \mathcal{GP}(0, K_1(x_1, x'_1; \theta_1)). \quad (15)$$

As shown in Figure 1, the low-fidelity power spectrum is biased high. We pass variations of the low-fidelity power spectrum around its mean to the next highest fidelity to avoid passing biased outputs. In practice, we found this slightly improves emulation accuracy for multi-fidelity models.

For the highest fidelity bias function,  $\delta_s(x)$ , we model the power spectrum using a zero mean GP without subtracting the sample mean. We do not have enough points at the highest fidelity for the sample mean to be a good estimate of the true mean. Except for  $t = 1$ ,  $f_t(x)$  is completely determined by  $f_{t-1}(x)$ ,  $\delta_t(x)$ , and  $\rho_t$ .

As mentioned by Kennedy & O’Hagan (2000), there is a Markov property implied in the covariance structure of Eq 12:

$$\text{cov}\{f_t(x), f_{t-1}(x') \mid f_{t-1}(x)\} = 0, \quad (16)$$

which is true for all  $x \neq x'$ . Eq 16 indicates that if we have  $f_{t-1}(x)$ , then other input parameters  $f_{t-1}(x')$  do not contribute to training  $f_t(x)$ .

The Markovian property also suggests that an efficient training set  $\{\mathcal{D}_1, \mathcal{D}_2, \dots, \mathcal{D}_s\}$  for a multi-fidelity GP is a nested structure:

$$\mathbf{x}_1 \subseteq \mathbf{x}_2 \subseteq \dots \subseteq \mathbf{x}_s. \quad (17)$$

The above notation says that, given an input point  $x$  at fidelity  $t$ , there must be an input  $x$  in its lower fidelity  $u$ , where  $u < t$  and  $t, u \in \{1, 2, \dots, s\}$ . The reason for using a nested experimental design is that since we have  $\mathbf{x}_{t-1} \subseteq \mathbf{x}_t$ , we can immediately get an accurate posterior  $f_{t-1}(x)$  at the  $x$  location without interpolating at the  $t - 1$  level. However, in practice we found our multi-fidelity emulators performed well even without a nested design in the input space.

At a given fidelity  $t$  and  $k = k_j$ , the posterior at a test input  $x_*$  could be written as

$$p(f_{*t} \mid \mathcal{D}, x_*) = \mathcal{N}(f_{*t}; \mu_{*t}(x_*), \sigma_{*t}^2(x_*)), \quad (18)$$

where we denote predictions from new inputs as subscript  $*$ . The predictive mean and variance are

$$\begin{aligned} \mu_{*t} &= \rho_t \cdot \mu_{*t-1}(x_*) + \mu \delta_t \\ &\quad + \mathbf{k}_{*n_t} \mathbf{K}_t^{-1} [\mathbf{y}_t - \rho_t \cdot \mu_{*t-1}(\mathbf{x}_t) - \mu \delta_t]; \\ \sigma_{*t}^2 &= \rho_t^2 \cdot \sigma_{*t-1}^2(x_*) + K(x_*, x_*) - \mathbf{k}_{*n_t} \mathbf{K}_t^{-1} \mathbf{k}_{*n_t}^\top, \end{aligned} \quad (19)$$

where  $\mathbf{k}_{*n_t} = [K_t(x_*, x_1), \dots, K_t(x_*, x_{n_t})]$  is a vector of covariance between the new location and the training locations at fidelity  $t$ .  $K_t = K_t(\mathbf{x}_t, \mathbf{x}'_t)$  is the covariance matrix of training locations at fidelity  $t$ .

#### 4.2.1 Covariance kernel

For a linear multi-fidelity emulator, we place an independent squared exponential kernel on each  $k_j$ :

$$K_t(x, x'; \boldsymbol{\theta}_t) = \sigma_t^2 \exp\left(-\frac{1}{2} \sum_{\ell=1}^d w_{t,\ell} (x_\ell - x'_\ell)^2\right). \quad (20)$$

$\sigma_t^2$  is the variance, and  $w_{t,\ell}$  is the ARD weights at  $\ell$ th input dimension at fidelity  $t$ .

Having ARD weights means we assign different length scales to each dimension so that the kernel can be trained

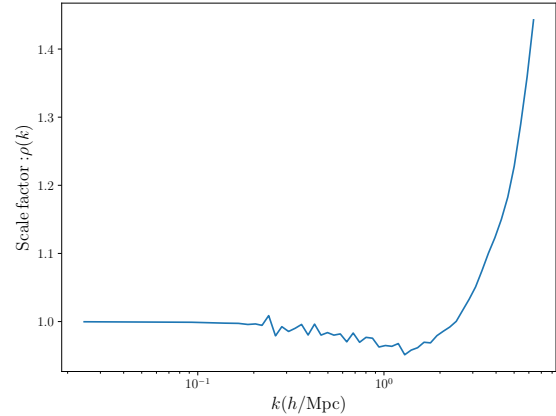


**Figure 2.** The learned scale factor between fidelities in the linear multi-fidelity model,  $\rho$ , as a function of  $k$ . This scale factor is learned from 50 low-fidelity simulations and 3 high-fidelity simulations.

anisotropically. We found that using ARD in the highest fidelity did not improve the model’s accuracy. Thus, we decided to assign an isotropic kernel for  $\delta_s$ . For a two-fidelity emulator with  $s = 2$ , we have 6 hyperparameters in low-fidelity for each  $k$  bin, where 5 of them are the length scale parameters and 1 is the variance parameter. We have 3 hyperparameters for each  $k$  bin in high fidelity, with one scale factor  $\rho_t$  between fidelities, one variance parameter, and one length scale parameter. We have 49 bins in  $k$ , so the total number of trainable hyperparameters is 441.

Figure 2 shows the learned scale factor,  $\rho_2$ , at each  $k$  mode.  $\rho_2$  is approximated to be unity at large scales  $k \leq 2 \text{ hMpc}^{-1}$ , but its value increases dramatically after  $k > 2 \text{ hMpc}^{-1}$ . Non-linear physics becomes important and the low-fidelity simulations become less reliable at small scales, making the relationship between fidelities non-trivial.

### 4.3 Non-linear multi-fidelity emulator (NARGP)

As in Section 4.2, we have simulated data  $\mathcal{D}_t = \{x_{i,t}, y_{i,t}\} = \{\mathbf{x}_t, \mathbf{y}_t\}$  for fidelity  $t = 1, \dots, s$  and simulations  $i = 1, \dots, n_t$ . The linear multi-fidelity model in Eq 12 assumes the scale factor  $\rho_t$  is  $x$  independent and so does not model the cosmological dependence of the scale factor  $\rho_t$ .

We use the non-linear multi-fidelity model proposed by Perdikaris et al. (2017) to allow the scale factor,  $\rho_t(\cdot)$ , to be a function of both input cosmology and output from the previous fidelity. As for the linear multi-fidelity model, we model the non-linear multi-fidelity GP independently for each  $k$ :

$$f_t(x) = \rho_t(x, f_{t-1}(x) - \mu_{t-1}) + \delta_t(x), \quad (21)$$

where  $\rho_t(\cdot)$  is a function of both input parameters  $x$  and the previous fidelity’s output.  $\rho_t(\cdot)$  is modelled as a GP. Eq 21 results in a more complicated distribution over  $f_t$ , a deep Gaussian process (Damianou & Lawrence 2013). To avoid added computational and statistical complexity, we follow the same approximation as Perdikaris et al. (2017) and replace  $f_{t-1}$  in Eq 21 with its posterior,  $f_{*t-1}$ . The result is a

regular Gaussian process,

$$f_t \sim \mathcal{GP}(0, K_t), \quad (22)$$

whose kernel can be furthermore decomposed:

$$K_t(x, x') = K_{t_\rho}(x, x'; \boldsymbol{\theta}_{t_\rho}) \cdot K_{t_f}(f'_{*t-1}(x), f'_{*t-1}(x'); \boldsymbol{\theta}_{t_f}) \\ + K_{t_\delta}(x, x'; \boldsymbol{\theta}_{t_\delta}), \quad (23)$$

where  $f'_{*t-1} \equiv f_{*t-1}(x) - \mu_{t-1}$  for simplicity. The first kernel  $K_{t_\rho}$  models the cosmological dependence of the scale factor  $\rho$ . Next,  $K_{t_f}$  models the covariance of the output passing from the previous fidelity to the current level. The final term  $K_{t_\delta}$  models the model discrepancy between fidelities. For the lowest fidelity, the matter power spectrum is only modelled with  $K_{t_\delta}$ .

Each kernel in Eq 23,  $(K_{t_\rho}, K_{t_f}, K_{t_\delta})$ , is modelled as a squared exponential kernel. Suppose we use ARD and assign a different length scale parameter for each  $x$  dimension.  $K_{t_\rho}$  will have  $d + 1$  hyperparameters,  $K_{t_f}$  will have 2 hyperparameters, and  $K_{t_\delta}$  will have  $d + 1$  hyperparameters. For a two-fidelity emulator with  $s = 2$ , we found no improvement in accuracy in practice by using ARD for the high-fidelity model. Thus, we have 2 hyperparameters for each kernel in high fidelity and  $d + 1$  hyperparameters for low-fidelity. To be explicit, in the high-fidelity model,  $K_{t_\rho}$  has 2 hyperparameters,  $K_{t_f}$  has 2 hyperparameters, and  $K_{t_\delta}$  has 2 hyperparameters. For  $d = 5$ , we have 6 hyperparameters for low-fidelity and 6 for a high-fidelity model at each  $k$  bin.

#### 4.3.1 Halo Model Interpretation

The formulation of a multi-fidelity emulator can be interpreted using a physically motivated model, the halo model. According to the halo model, all matter in the Universe is contained in dark matter haloes. Thus, we can decompose the matter power spectrum into one- and two-halo terms. The correlation between two distinct haloes is modelled by the two-halo term, which controls the power spectrum on large scales. The correlation within a single halo is modelled by the one-halo term, which dominates on small scales. For our multi-fidelity emulators in Eq 12 (AR1) and Eq 21 (NARGP), the correlations between fidelities are strong on large scales, and the two-halo term will be learned by the scaling factor  $\rho$ . On small scales, the bias  $\delta(\cdot)$  is used to compensate for the discrepancy between fidelities. The bias function is essentially calibrating the one-halo term using high-fidelity simulations.

## 5 SAMPLING STRATEGY FOR HIGH-FIDELITY SIMULATIONS

In this section, we will describe how we select the training simulations for our multi-fidelity emulators. We will first describe the nested structure implemented in multi-fidelity emulators in Section 5.1. Section 5.2 explains how we find the optimal choice of high-fidelity training simulations.

### 5.1 Nested training sets

The proposed sampling scheme for training and testing is shown in Figure 3. The corresponding output power spectra

are shown in Figure 4. In Figure 3, the sampling is done using two different Latin hypercubes:

- (i) Training simulations: a Latin hypercube with 50 points. HR points are a subset of LR points.
- (ii) Testing simulations: another Latin hypercube with 10 points.

The first hypercube with 50 points ensures that we will have a nested experimental design. The second hypercube is to ensure we will not test on the training simulations during the validation phase. In practice, we found that the emulation accuracy roughly converged with  $\sim 30$  LR points.

### 5.2 Optimize the loss of low-fidelity simulations

For a multi-fidelity problem, we want to minimize the required high-fidelity training simulations. To avoid selecting HR points that are crowded in the parameter subspace, we search for the optimal set of HR points. We pick the subset that would minimize the low fidelity training set's single-fidelity emulator errors. In our experiments with two fidelities,  $s = 2$ , there are  $\binom{n_1}{n_2}$  possible combinations for  $\boldsymbol{x}_2$ , which are input parameters for the high-fidelity data,  $\mathcal{D}_2 = \{\boldsymbol{x}_2, \boldsymbol{y}_2\}$ .

Consider  $\mathcal{S}$ , a potential  $\mathcal{D}_2$  with  $\boldsymbol{x}_2 \subset \boldsymbol{x}_1$ . We train a low-fidelity only emulator based on Eq 7 using these  $n_2$  low-fidelity points and get a GP conditioned on  $\mathcal{S}$ :

$$p(f_* | \mathcal{S}, x_*) = \mathcal{N}(f_* | \mu_*^{(i)}(x_*), \sigma_*^{(i)}(x_*)^2), \quad (24)$$

which is the posterior as described in Eq 8.

With the trained low-fidelity only emulator in Eq 24, we can test this single-fidelity emulator's performance by predicting the rest of the data in the low-fidelity Latin hypercube. To evaluate the accuracy, we compute the mean squared error by averaging over the test data:

$$\text{MSE} = \mathbb{E}[(y_* - \mu_*^{(i)}(x_*))^2], \quad (25)$$

where  $\{(x_*, y_*)\}$  are the low-fidelity data pairs from the rest of the Latin hypercube,

$$\{(x_*, y_*)\} \in \{\mathcal{D}_1 - \mathcal{S}\}. \quad (26)$$

This simply means that we test the single-fidelity emulator on the available data not included in the training subset.

Suppose we repeat the training of single-fidelity emulators until we train all possible subsets in the low-fidelity hypercube. We will now have  $\binom{n_1}{n_2}$  trained single-fidelity emulators. Each single-fidelity emulator will provide a mean squared error, which is the test error that the emulator generates against the low-fidelity hypercube test data. To select the optimally trained emulator, we compute

$$\mathcal{S}^* = \arg \min_{\mathcal{S}^*} (\mathbb{E}[(y_* - \mu_*^{(i)}(x_*))^2]), \quad (27)$$

where we find the subset  $\mathcal{S}^*$  which minimizes the mean squared errors on the test set. We use  $\mathcal{S}^*$  as our high-fidelity training set  $\mathcal{D}_2$  under the nested experimental design. To be explicit:

$$\boldsymbol{x}_2 = \boldsymbol{x}_{\mathcal{S}^*} \subset \boldsymbol{x}_1, \quad (28)$$

where  $\boldsymbol{x}_2$  are the selected high-fidelity input points,  $\boldsymbol{x}_{\mathcal{S}^*}$  are the input points from the selected subset  $\mathcal{S}^*$  (which minimize the low-fidelity emulator mean squared error), and  $\boldsymbol{x}_1$  are the low-fidelity input points.



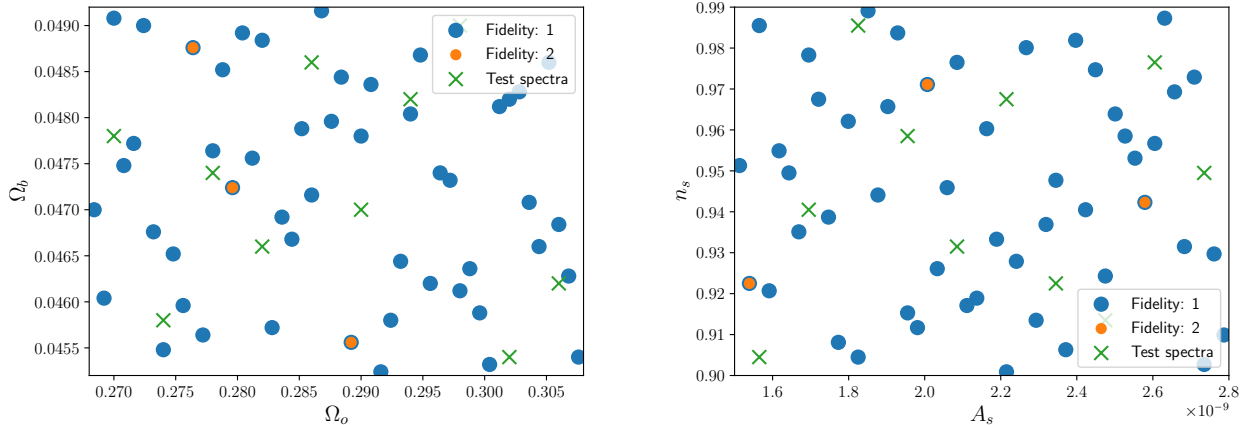


**Figure 3.** Two 2-D cross-sections of the 5-D samples of input parameters. The input parameters are designed with a nested structure,  $\mathbf{x}_1 \propto \mathbf{x}_2$ , between HR and LR. **(Blue):**  $\mathbf{x}_1$ , 50 sampling points in LR. **(Orange):**  $\mathbf{x}_2$ , 3 sampling points in HR. The selection of these 3 points is chosen by the procedure described in Section 5.2, which minimizes the LR error in the low-fidelity only emulator. **(Green):** 10 points from the HR testing set, which is a different Latin hypercube than  $\mathbf{x}_1$

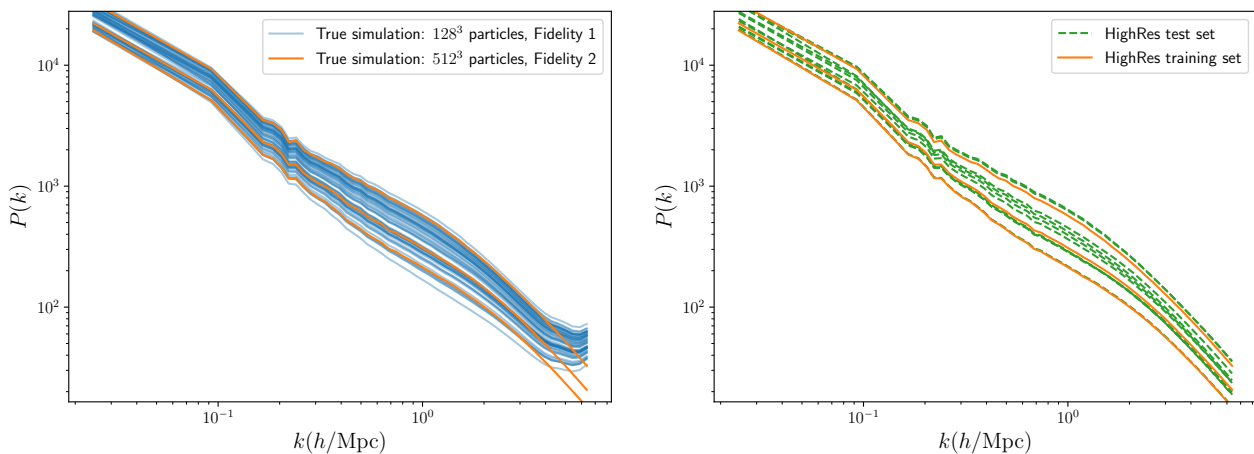


**Figure 4.** Training (left) and testing (right) data for the multi-fidelity emulator. **(Left):** 50 low-fidelity training simulations (blue) and 3 high-fidelity simulations (orange) used in a 50LR-3HR emulator. A HR is a  $512^3$  simulation and a LR is a  $128^3$  simulation. Both HR and LR are in a box with 256 Mpc/h per side. The 50 low-fidelity training simulations are drawn from a 5D Latin hypercube,  $(h, \Omega_0, \Omega_b, A_s, n_s)$ . The 3 high-fidelity simulations are a subset of the low-fidelity simulation hypercube. **(Right):** 10 high-fidelity test simulations (green dashed) and 3 high-fidelity training simulations (orange).

This strategy assumes that the effect of a sampling scheme on a low-fidelity emulator is the same as that on a corresponding multi-fidelity emulator. For example, suppose  $\Delta\Omega_b$  is crucial for learning how the low-fidelity power spectrum  $y_1$  changes for inputs  $x_1$ . In that case, we expect that information about  $\Delta\Omega_b$  can also effectively change the high-fidelity spectrum  $y_2$ .

The above assumption could be violated if the power spectra at small scales, which are not included in the low-fidelity data, behave very differently from those at large scales. This could happen if the smoothness length scale acts very differently between low-fidelity and high-fidelity data for a given input dimension. For example, imagine that a parameter,  $\theta$ , has a small effect on the outcomes of low-fidelity simulations, but a large effect on the outcomes of high-fidelity simulations.

Figure 5 shows the mean squared errors computed from  $64^3$  single-fidelity emulators and  $256^3$  single-fidelity emulators. First, note that the selection of the training simulations affects the emulator accuracy. Second, the low-fidelity emulator errors are correlated with their higher fidelity counterparts. This suggests that a low-fidelity emulator can serve as a guide for placing high-fidelity training simulations. The HR parameter choices used in Section 6 were selected with an earlier version of our model using  $64^3$  particle simulations. We checked that using either  $64^3$  or  $128^3$  for selection gave almost the same emulation accuracy for a non-linear 50 LR-3 HR emulator, though one of the selected samples is different.

In practice, we find the procedure above can prevent us from selecting the HR combination that will give us the worst multi-fidelity emulation result. Although we have tested that

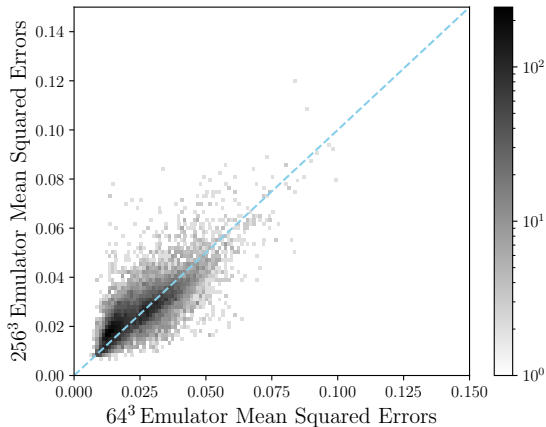


**Figure 5.** Emulator mean squared errors evaluated from  $64^3$  emulators and  $256^3$  emulators. We compute all subsets of 3 samples from a 50 samples Latin hypercube,  $\binom{50}{3} = 19600$  subsets in total. Colorbar is in log scale. The blue dashed line represents a perfect linear relationship.

our procedure works for the matter power spectrum, we would suggest that when emulating a new summary statistic (e.g., the halo mass function), the reader investigates the effectiveness of this method using small test cases. The training of  $\binom{50}{2} = 1225$  low-fidelity emulators (select two samples out of 50 points) could also be a computationally consuming task. To save computational cost, we employed a greedy optimization strategy. Instead of exploring all possible subsets, we grew the subset one point at a time, fixing the previously chosen points. Also, we used the same set of kernel parameters for all  $k$  bins to decrease the computational requirements. We may investigate using Bayesian optimization (e.g., Forrester et al. (2007); Lam et al. (2015); Poloczek et al. (2016)) to select the optimal HR samples for multi-fidelity training in future work.

## 6 RESULTS

This section shows the interpolation accuracy of multi-fidelity methods and compares our multi-fidelity emulators to single-fidelity emulators. Section 6.1 compares test set emulator errors for the linear multi-fidelity emulator (AR1) and non-linear multi-fidelity emulator (NARGP). Section 6.2 compares a multi-fidelity emulator with two kinds of single-fidelity emulators, including high-fidelity only emulators and low-fidelity only emulators. We also compare the emulator accuracy as a function of core hours for both multi-fidelity emulators and single-fidelity emulators.

To test how much a multi-fidelity emulator can improve with more training simulations, Section 6.3 shows the emulator errors with more LR or HR training simulations. Finally, Section 6.4 checks the performance of the multi-fidelity method for other emulation settings.

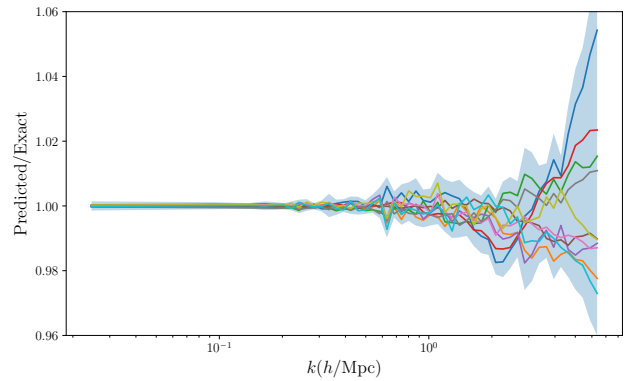


**Figure 6.** Predicted divided by exact power spectrum from a 50 LR-3HR emulator using a linear multi-fidelity method (AR1). Different colours correspond to 10 test simulations spanning a 5-D Latin hypercube. The shaded area indicates the worst-case  $1 - \sigma$  emulator uncertainty. There is one test simulation driving the larger error compared to the non-linear one in Figure 7.

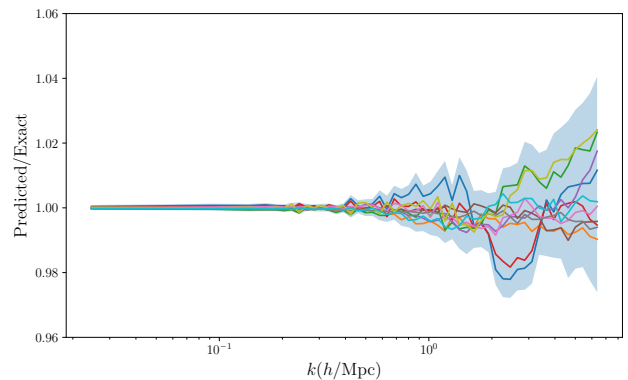


**Figure 7.** Predicted divided by exact power spectrum from a 50 LR-3HR emulator using a non-linear multi-fidelity method (NARGP). Different colours correspond to 10 test simulations spanning a 5-D Latin hypercube. The shaded area indicates the worst-case  $1 - \sigma$  emulator uncertainty. Note that the y-scale in this plot is the same as Figure 6.

### 6.1 Comparison of Linear and Non-Linear Emulators

Figure 6 and Figure 7 show the predicted power spectrum divided by the exact power spectrum for simulations in the testing set. Both emulators, linear (AR1) and non-linear (NARGP), are trained with 50 low-fidelity simulations and 3 high-fidelity simulations. We will call these emulators “50 LR-3HR emulators” for simplicity. A non-linear multi-fidelity emulator requires at least 3 HR simulations for training and has  $\lesssim 2\%$  worst-case accuracy per  $k$  bin. For a linear multi-fidelity emulator, the minimum required number of HR simulations needed is 2, reflecting the lower number of hyperparameters in the kernel.

Figure 8 shows a comparison between a linear multi-fidelity emulator and a non-linear multi-fidelity emulator in relative emulator error. We include linear and non-linear 50 LR-3HR emulators with an additional linear 50 LR-2HR emulator in the plot. The definition of the relative emulator

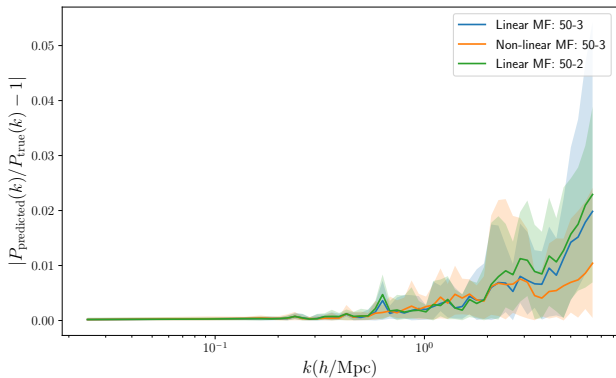


**Figure 8.** Relative emulator errors from a 50 LR-3 HR emulator using linear multi-fidelity (blue) and non-linear multi-fidelity (orange). We also include a linear 50 LR-2 HR emulator (green). Solid lines represent the average error from test simulations,  $\frac{1}{10} \sum_{i=1}^{10} | \frac{P_{\text{pred},i}}{P_{\text{true}}} - 1 |$ . Shaded areas show the maximum and minimum test errors.

error is:

$$\text{Emulator Error} = \left| \frac{P_{\text{pred}}}{P_{\text{true}}} - 1 \right|. \quad (29)$$

$P_{\text{pred}}$  is the predicted power spectrum from the multi-fidelity emulator, and  $P_{\text{true}}$  is the power spectrum from the simulation.

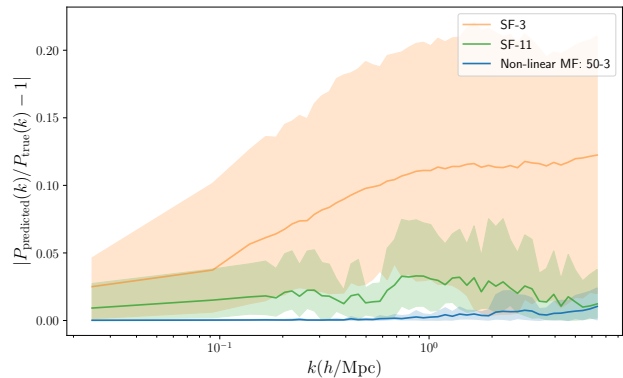
Figure 8 shows that the linear 50 LR-3 HR emulator predicts an average error  $< 1\%$  per  $k$  bin for  $k \leq 4 \text{ hMpc}^{-1}$  and  $< 2\%$  per  $k$  bin for  $4 < k \leq 6.4 \text{ hMpc}^{-1}$ . For the non-linear multi-fidelity emulator, it predicts an average error  $\lesssim 1\%$  per  $k$  bin, which implies we only need 3 HR to achieve a percent-level accurate emulator using the non-linear multi-fidelity method. At  $k \leq 3 \text{ hMpc}^{-1}$ , both emulators predict mostly the same accuracy, but the non-linear one performs better at smaller scales  $k > 3 \text{ hMpc}^{-1}$ .

Figure 8 shows a linear 50 LR-2 HR emulator makes a  $< 5\%$  accuracy prediction with only 2 HR available. A linear multi-fidelity has fewer hyperparameters than a non-linear multi-fidelity, so it is trainable with only 2 HR. We found that the non-linear multi-fidelity emulator outperforms the linear one in all aspects. For simplicity, we will only show the non-linear multi-fidelity models in the following sections, but we note that a linear multi-fidelity model is still useful when only two HR simulations are available.

## 6.2 Comparison to single-fidelity emulators

### 6.2.1 Comparison to high-fidelity only emulators

Figure 9 shows a comparison between a non-linear 50 LR-3 HR emulator and high-fidelity only emulators. The high-fidelity only emulators are single-fidelity emulators trained solely on HR simulations. The non-linear multi-fidelity emulator outperforms the single-fidelity emulator with 11 HR at all  $k$  modes. It also predicts a worst-case error smaller than the worst-case error from the 11 HR single-fidelity emulator. At  $k \leq 2 \text{ hMpc}^{-1}$ , the multi-fidelity emulator performs much better than the single-fidelity emulators. Since LR simulations can predict accurate power spectrum at large scales  $k \leq 2 \text{ hMpc}^{-1}$ , we expect a single-fidelity emulator re-



**Figure 9.** Non-linear multi-fidelity emulator (blue) with 50 LR and 3 HR simulations, compared to single-fidelity emulators with 3 HR (orange) and with 11 HR (green). Shaded area indicates the maximum and minimum emulation errors. The computational cost for a 50 LR-3 HR emulator is 9 000 core hours while the single-fidelity emulator with 11 HR requires 25 000 core hours. However, a 50 LR-3 HR emulator still outperforms an 11 HR emulator.

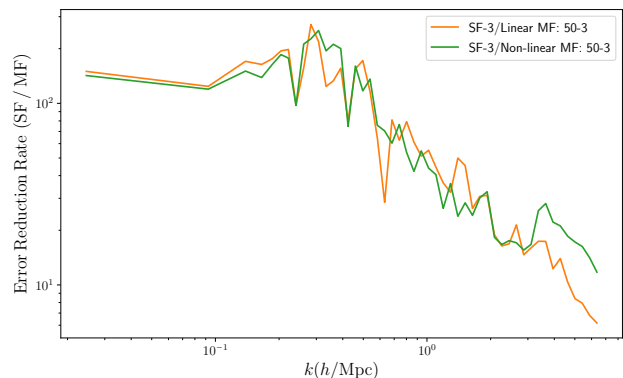


**Figure 10.** Error reduction rate from single-fidelity to multi-fidelity emulator. We fix the number of HR simulations to 3, and calculate the reduction of average emulator errors from a linear 50 LR-3 HR emulator (orange) and a non-linear 50 LR-3 HR emulator (green). A larger reduction rate implies a better multi-fidelity emulator at a given scale.

quires  $\sim 50$  HR to compete with the 50 LR-3 HR emulator on large scales. A HR is  $\simeq 64$  times more expensive than a LR, thus the core time for a 50 LR-3 HR emulator is  $\simeq 4$  HR. The non-linear multi-fidelity outperforms a single-fidelity 11 HR emulator with  $\simeq 3$  times lower computational cost.

Figure 10 depicts the error reduction rate between a 50 LR-3 HR emulator and a 3-HR single-fidelity emulator. Both linear and non-linear emulators show an error reduction rate of  $\simeq 100$  for  $k \leq 0.5 \text{ hMpc}^{-1}$ ,  $\simeq 100$  times better than the single-fidelity counterpart. At smaller scales  $k > 3 \text{ hMpc}^{-1}$ , the multi-fidelity emulators are  $\simeq 20$  times (non-linear), and  $\simeq 10$  times (linear) better than their single-fidelity counterpart.

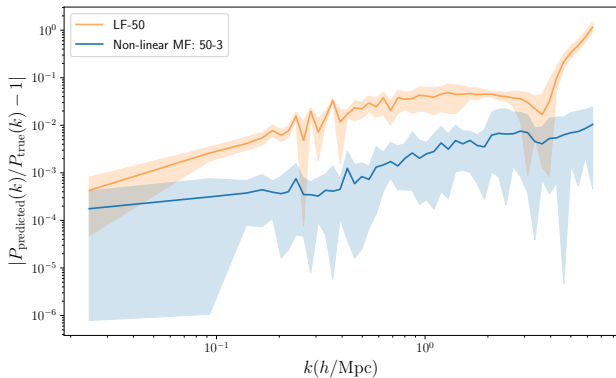


**Figure 11.** Relative emulator errors between a 50 low-fidelity emulator and a non-linear 50 LR-3 HR emulator. Errors are evaluated on 10 HR simulations. Shaded area indicates the maximum and minimum errors. Note that the y-axis is in  $\log_{10}$  scale.

### 6.2.2 Comparison to low-fidelity only emulators

Figure 11 shows a single-fidelity emulator trained on 50 LR simulations, compared to a non-linear 50 LR-3 HR emulator. Figure 11 demonstrates how multi-fidelity modelling improves the emulator accuracy on each  $k$  scale. At  $k \lesssim 3 h\text{Mpc}^{-1}$ , multi-fidelity modelling uses 3 HR to correct the resolution and reduce the average emulator error from  $\lesssim 5\%$  to  $\leq 1\%$ . A low-fidelity emulator predicts a biased power spectrum beyond  $k = 3 h\text{Mpc}^{-1}$ . However, the multi-fidelity method can moderately correct the bias and reduce the error to  $\lesssim 1\%$ . Again, the multi-fidelity technique can use a few HR simulations to calibrate the resolution difference.

### 6.2.3 Core hours versus emulator errors

Figure 12 shows the average relative emulator error as a function of core hours for performing the training simulations. The emulator errors shown in Figure 12 are averaged over all  $k$  modes, so each emulator corresponds to a single point in the plot. An ideal emulator will be on the left bottom corner, implying both low cost and high accuracy. The slope of a given emulator in the plot indicates how easily we can improve the emulator with more training data. A steeper (more negative) slope means we can increase the emulator accuracy with a lower cost.

We notice three types of emulators are clustered in separate regions in the plot. The low-fidelity only emulator (LF-only) has the lowest cost and shows no noticeable improvement from increasing training simulations from 50 to 400 LR. The high-fidelity only emulator (HF-only) shows an accuracy improvement with more HR simulations from 3 HR to 11 HR. However, performing one HR requires  $\sim 2000$  core hours, making the HF-only emulator much more expensive than the other two emulators in the plot.

In Figure 12, the non-linear multi-fidelity emulator (NARGP) shows a compute time similar to 3 HR simulations but has better accuracy than the HF-only emulator. It also presents a steeper slope than the HF-only emulator, indicating we can efficiently increase the accuracy using low-cost LR simulations. From 10 LR-3 HR emulator to 50 LR-3 HR emulator, it shows that we can decrease the error from

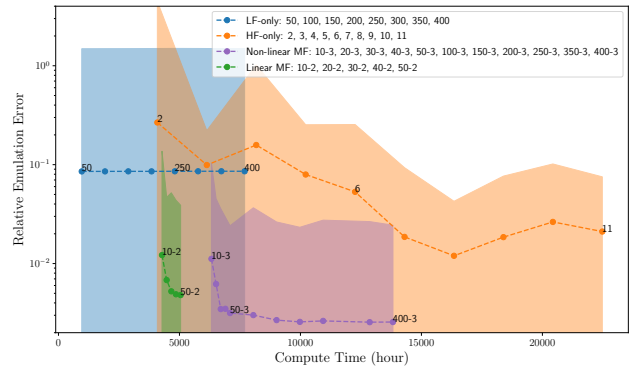


**Figure 12.** Core hours for running the training simulations versus emulation errors for high-fidelity only emulators (orange) and low-fidelity only emulators (blue), linear multi-fidelity emulators (AR1) with 2 HR (green), and non-linear multi-fidelity emulators (NARGP) with 3 HR (purple). The numbers in the labels indicate the number of training simulations used in the emulator. For example, the numbers after LF-only emulator mean how many low-resolution simulations used in the emulator. For multi-fidelity emulators,  $X$ - $Y$ ,  $X$  is the number of low-resolution and  $Y$  is the number of high-resolution training simulations. The dots show the average errors. The upper shaded areas show the maximum emulator errors among 10 test simulations. The LR samples beyond 100 are drawn from a separate Latin hypercube with 400 samples.

$\sim 0.02$  to  $\sim 0.003$  using an additional  $\sim 800$  core hours. From 50 LR-3 HR emulator to 400 LR-3 HR emulator, we also see a mild decrease of error but not as steep as 10LR-3HR to 50LR-3HR.

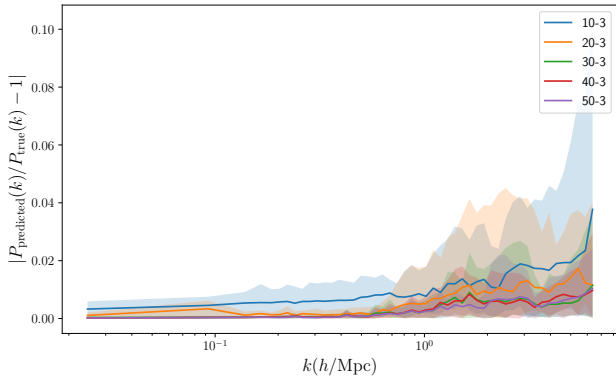
We also include the linear model (AR1) to demonstrate the performance of the multi-fidelity method when there are only 2 HR available. The linear model also shows a steep improvement slope from 10LR-2HR to 50LR-2HR. However, we notice that the linear model with 2 HR is slightly worse than the non-linear one with 3 HR.

Figure 12 demonstrates that a multi-fidelity emulator can provide good accuracy with a much lower cost than HF-only emulators. It also points out that we can efficiently improve the accuracy of a multi-fidelity emulator using cheap low-fidelity simulations.

## 6.3 Varying the number of training simulations

### 6.3.1 Effects of more low-resolution training simulations

The benefit of using a multi-fidelity emulator is that we can improve the emulator accuracy using extra low-fidelity simulations. Figure 13 shows the emulator error colour coded by the number of LR training simulations. With more LR training data, the emulator performance improves at both large and small scales. We only show the non-linear emulator here for simplicity, but we observe a similar trend in the linear emulator. For  $N_{\text{LR-3HR}}$  with  $N \in \{10, 20, 30, 40, 50\}$  emulators, the last  $k$  bin gives 3.77%, 1.16%, 1.15%, 0.97%, and 1.04% emulator errors, indicating an increase of accuracy with more LR training simulations. Dividing the errors into large and small scales at  $k = 1 h\text{Mpc}^{-1}$ , the average emulator errors are 0.65%, 0.22%, 0.10%, 0.09%, and 0.09% for  $k \leq 1 h\text{Mpc}^{-1}$  and 1.60%, 1.04%, 0.60%, 0.61%, and 0.56%



**Figure 13.** Relative emulator error of non-linear  $N$  LR-3 HR emulator colour coded with different number of LR training simulations, with  $N \in \{10, 20, 30, 40, 50\}$ . The same as Figure 8, solid lines represent the average error from test simulations,  $\frac{1}{10} \sum_{i=1}^{10} |j \frac{P_{\text{pred},i}}{P_{\text{true}}} - 1|$ , and shaded areas show the maximum and minimum test errors.

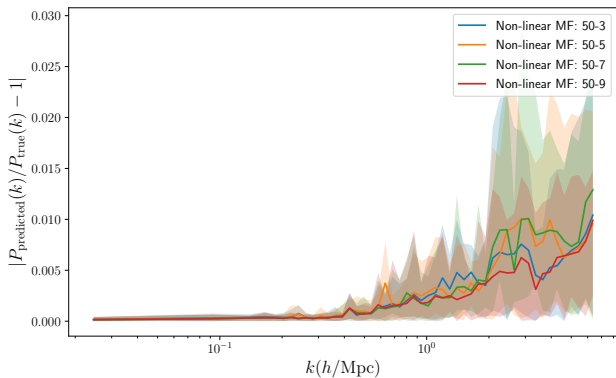


**Figure 14.** Relative emulator errors from non-linear 50 LR- $N$  HR emulator with  $N = 3$  (blue),  $N = 5$  (orange),  $N = 7$  (green), and  $N = 9$  (red) HR training simulations. Solid lines are the average test errors. Shaded areas show the maximum and minimum test errors.

for  $k > 1 \text{ hMpc}^{-1}$ . The decrease in error is nearly saturated with  $\sim 40$  LR simulations.

### 6.3.2 Effects of more high-resolution training simulations

In Figure 14, we add more HR training simulations to our multi-fidelity emulator. The 50 LR- $N$  HR emulator with  $N \in \{3, 5, 7, 9\}$  shows no apparent improvement with more HR, except the 50 LR-9 HR emulator is marginally better than others. One reason may be stochasticity in the training set due to simulation modelling error, which is around 1%, and limits the prediction accuracy. In particular, MP-GADGET simulations with  $512^3$  particles may not be fully converged on small scales, and this limits the emulator’s learning. Another possibility is that the prior from 50 low-fidelity simulations may be too hard to overcome with only 9 HR simulations.

To improve multi-fidelity emulator accuracy further, one could build a more complicated model than the one proposed in this paper. The improvement from the linear

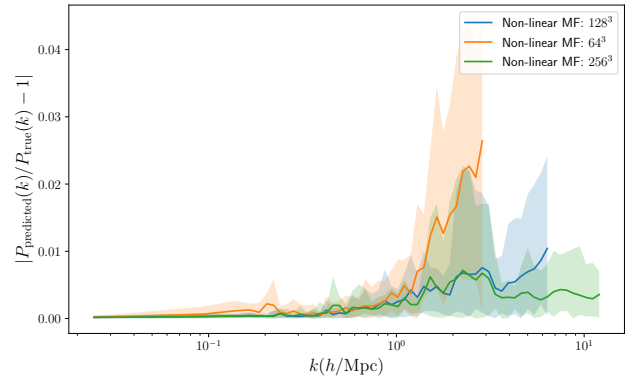


**Figure 15.** Relative emulator errors for 50 LR-3 HR emulator emulators using different qualities of LR simulations. **(Blue)**: using  $128^3$  simulations as low-fidelity training simulations. **(Orange)**: using  $64^3$  simulations as LR, which are  $\sim 8$  times cheaper than  $128^3$  simulations. **(Green)**: using  $256^3$  simulations as LR, which are  $\sim 8$  times most expensive than  $128^3$  simulations. Shaded area shows the maximum and minimum errors among ten test simulations.

to the non-linear model shows that different decisions about the scaling factor  $\rho$  could better predict the non-linear structure. However, those complicated models will require more high-fidelity training simulations. We will leave more complex modelling structures to future work.

## 6.4 Effect of other emulation parameters

### 6.4.1 The resolution of low-fidelity simulations

We have so far tested multi-fidelity emulators using  $128^3$  simulations (LR) as low-fidelity and  $512^3$  simulations (HR) as high-fidelity. Figure 15 shows non-linear 50 LR-3 HR emulators using different mass resolutions,  $64^3$  and  $256^3$  simulations, as low-fidelity.

A  $64^3$  simulation is  $\simeq 512$  times cheaper than a HR but has a smaller maximum  $k$  with  $\max(k) \simeq 3 \text{ hMpc}^{-1}$ . It produces percent level accuracy for  $k \leq 1 \text{ hMpc}^{-1}$  and has worst-case errors  $< 5\%$  at small scales  $k \geq 1 \text{ hMpc}^{-1}$ . A  $256^3$  simulation is  $\simeq 8$  times cheaper than a HR simulation, so the computational cost for a 50 LR-3 HR emulator is  $\simeq 9$  HR simulations. This emulator mildly outperforms the emulator where LR is  $128^3$  for  $k > 3 \text{ hMpc}^{-1}$ , with an average percent-level emulation until  $k \simeq 12 \text{ hMpc}^{-1}$ , but at a substantially increased computational cost. Figure 9 shows it still has substantially improved accuracy than a single fidelity emulator with 9 HR simulations, which has similar computational cost.

Figure 15 demonstrates that one can fuse various qualities of LR with HR simulations to build a multi-fidelity emulator. Figure 15 also shows that the multi-fidelity emulator’s accuracy depends on the correlation between LR and HR. A  $64^3$  simulation is only a rough approximation to its  $512^3$  counterpart, so the emulator that uses  $64^3$  simulations as low-fidelity is less accurate than the others in Figure 15.

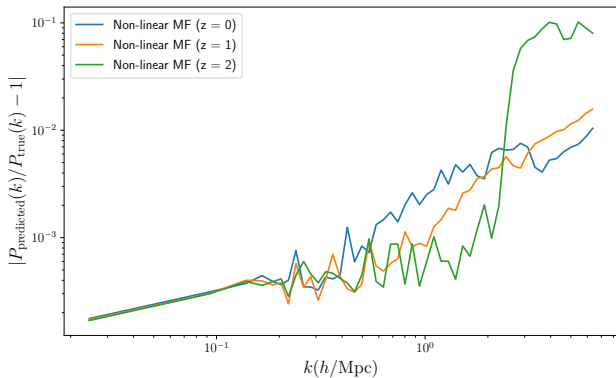


**Figure 16.** Relative emulator errors for a non-linear emulator at different redshifts,  $z \in \{0, 1, 2\}$ . Note the y-axis is in  $\log_{10}$  scale. The larger error in the  $z = 2$  emulator at  $k > 2 h\text{Mpc}^{-1}$  may be due to a transient near the mean-particle spacing in the LR simulations, see Figure 17.

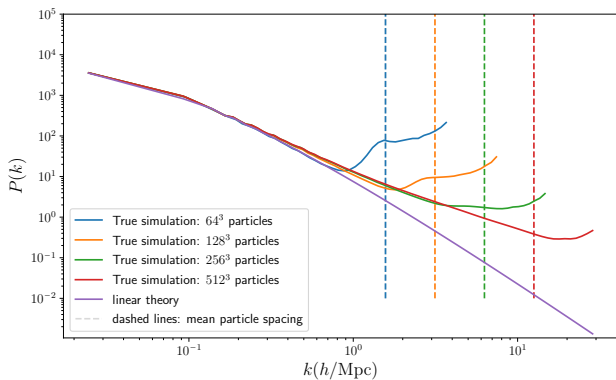


**Figure 17.** The matter power spectrum at  $z = 2$ , output by MP-GADGET with different mass resolutions. The vertical dash lines indicated the mean particle spacing  $k_{\text{spacing}}$  for a given mass resolution. **(Blue):** The matter power spectrum from dark-matter only MP-GADGET simulation with  $N_{\text{ptl,side}} = 64$ . **(Orange):** The matter power spectrum from MP-GADGET with  $N_{\text{ptl,side}} = 128$ . **(Green):** The matter power spectrum from MP-GADGET with  $N_{\text{ptl,side}} = 256$ . **(Red):** The matter power spectrum from MP-GADGET with  $N_{\text{ptl,side}} = 512$ . **(Purple):** Linear theory power spectrum.

#### 6.4.2 Emulation at $z = 1$ and $z = 2$

This section examines the performance of a non-linear emulator at higher redshifts,  $z = 1$  and  $z = 2$ . Figure 16 shows the emulator error of a non-linear 50 LR-3 HR emulator at  $z = 0, 1, 2$ . The mean error at  $z = 1$  is smaller than the  $z = 0$  error at  $k \leq 2 h\text{Mpc}^{-1}$  while it is larger for  $k > 2 h\text{Mpc}^{-1}$ . This result shows that it is easier to train the correlation between fidelities at large scales  $k \leq 2 h\text{Mpc}^{-1}$  while harder to train at small scales  $k > 2 h\text{Mpc}^{-1}$ . The emulator at  $z = 2$  also shows a better performance than  $z = 0$  at large scales,  $k \leq 2 h\text{Mpc}^{-1}$ , but the error diverges to  $\sim 10\%$  on smaller scales,  $k > 2 h\text{Mpc}^{-1}$ . The improved performance on large scales may be because at higher redshifts the matter power spectrum is closer to linear theory and so the correlation between fidelities is easier to learn.

Figure 17 shows the matter power spectrum at  $z = 2$ ,

with the same cosmological parameters as Figure 1 and indicates a potential explanation. At  $z = 2$ , the low-fidelity simulation contains a systematic at the scale of the mean interparticle spacing, related to the initial spacing of particles on a regular grid. This systematic is a transient and disappears by  $z = 0$ . However, at redshifts where it is present it implies that the low fidelity simulations contain very little cosmological information on scales near their mean interparticle spacing,  $k \simeq 3 h\text{Mpc}^{-1}$  and thus cannot significantly improve the emulation accuracy. It may be possible to improve performance at high redshift with the use of other pre-initial conditions such as a Lagrangian glass (White 1994).

## 7 RUNTIME

We ran our simulations using MP-GADGET on UCR’s High Performance Computing Center (HPCC) and the Texas Advanced Computing Center (TACC). The standard computational setup was 256 MPI tasks per simulation for both HR ( $512^3$  dark matter particles) and LR ( $128^3$  dark matter particles). The runtime was  $\sim 20$  core hours for LR and  $\sim 2000$  core hours for HR, with a fixed boxsize  $256 \text{ Mpc}/h$ . The computational time for a  $64^3$  simulation was  $\sim 1.5$  core hours with 64 MPI ranks and  $\sim 280$  core hours for a  $256^3$  simulation with 256 MPI ranks.

The computational cost for training a non-linear 50 LR-3 HR emulator (NARGP) was  $\simeq 0.5$  hours and  $\simeq 1.6$  hours for a linear 50 LR-3 HR emulator (AR1) on a single core. For a single-fidelity emulator, it was  $\simeq 2$  minutes on one core. The compute time could be further improved by parallelizing the hyperparameter optimization for each  $k$  bin. The compute time for optimizing the choice of HR using low-fidelity emulators was  $\sim 3$  hours for selecting 3 HR (on one core). The run time was  $\simeq 12$  seconds for evaluating 10 test simulations.

## 8 CONCLUSIONS

We have presented multi-fidelity emulators for the matter power spectrum. Multi-fidelity methods fuse together  $N$ -body simulations from different mass resolutions to improve interpolation accuracy. Multi-fidelity emulators use many low-fidelity simulations to learn the power spectrum’s dependence on cosmology, correcting for their low resolution by adding a few high-fidelity simulations. The result is equivalent in accuracy to a single-fidelity emulator with much more costly high-fidelity simulations. A multi-fidelity emulator’s physical motivation can be understood using the halo model: low-fidelity simulations capture the two-halo term at large scales, while a few high-fidelity simulations are used to learn the (almost cosmology independent) one-halo term at small scales.

We have also proposed a new sampling strategy which uses low-fidelity simulations as a prior to place high-fidelity training simulations. We choose our high-fidelity training samples by optimizing the low-fidelity emulator’s error. In this way, the input parameters at which to run HR simulations can be optimized without knowledge of the HR output. We showed that single-fidelity emulator errors are correlated between different fidelities, indicating that a lower fidelity

emulator can serve as a good prior for picking HR simulation points.

Our best multi-fidelity emulator achieved percent level accuracy using only 3 HR simulations and 50 LR simulations, with a total computational cost  $\lesssim 4$  HR simulations. We showed it outperforms a single-fidelity emulator with 11 HR simulations. We expect that a single-fidelity emulator would require  $\sim 50$  HR simulations to compete with the multi-fidelity one at  $k \leq 2 h\text{Mpc}^{-1}$ .

We used simulations with  $128^3$  particles as our low-fidelity training sample and simulations with  $512^3$  particles as high-fidelity, with a fixed  $256 \text{Mpc}/h$  box. We tested our emulator with a series of 10 HR simulations in a Latin hypercube. We used two types of multi-fidelity emulators, linear (AR1) and non-linear (NARGP). We showed that both emulators perform similarly at large scales, while the non-linear one has a better accuracy at small scales.

We focussed on  $z = 0$ , but also investigated higher redshifts. Higher redshift power spectra behave more linearly than at  $z = 0$ , so it is easier to learn the large-scale correlation between fidelities. However, the low-fidelity power spectra are less reliable beyond the mean particle spacing at higher redshifts, inducing some difficulty modelling small scales with  $k > 2 h\text{Mpc}^{-1}$ .

Our multi-fidelity emulators could provide percent-level predictions for future space- and ground-based surveys at a minimum computational cost. All current emulators are single-fidelity, training only on expensive high-fidelity simulations. A single-fidelity emulator requires at least  $\sim 40$  simulations to give percent-level accuracy in a  $\Lambda\text{CDM}$  Universe. For example, Heitmann et al. (2009) use 37 simulations to emulate a 5-dimensional  $\Lambda\text{CDM}$  model. Euclid Collaboration et al. (2020) use  $\sim 200$  high-fidelity simulations ( $3000^3$  dark matter particles) to achieve the upcoming Euclid mission's desired accuracy in an 8 dimensional parameter space.

Our multi-fidelity methods can also be used to improve the existing single-fidelity emulators. For example, suppose we have run 50 high-resolution simulations to build an emulator. We can perform 3 additional super high-resolution simulations and combine them to build a multi-fidelity emulator. The choice of these 3 simulations could be selected via the optimization strategy proposed in this paper. Instead of performing super high-resolution simulations, one could use super-resolution techniques (see Li et al. 2020) to generate super-resolution simulations and combine them with a multi-fidelity emulator.

In this work, we only test our multi-fidelity emulators with  $512^3$  resolution and a relatively small box  $256 \text{Mpc}/h$ . In future work we will apply the framework developed here to create a real production emulator using higher particle load simulations (e.g.,  $2048^3$  particles) in larger boxes. Other summary statistics, including the halo mass function and the cosmic shear power spectrum, could also be emulated using the same framework.

The multi-fidelity framework may also be extended to hydrodynamical simulations, which are much more costly than their dark matter only counterparts. No production hydrodynamical emulators including galaxy formation effects such as AGN feedback yet exist.<sup>11</sup> However, AGN

feedback significantly affects the matter power spectrum at  $k > 0.1 h\text{Mpc}^{-1}$  (van Daalen et al. 2011) and pressure forces can affect the power spectrum at  $k \sim 10 h\text{Mpc}^{-1}$  (White 2004). Thus practical exploitation of the small-scale information from future surveys will require the development of hydrodynamical emulators. By decreasing the computational cost of an emulator by a factor of  $\approx 3$  and still outperforming the single-fidelity emulator, the work presented here makes emulation development substantially more practical.

## SOFTWARE

We used the GPy package for Gaussian processes. For multi-fidelity kernels, we moderately modified the multi-fidelity submodule from `emukit`.<sup>12</sup> We used the MP-GADGET software for simulations.<sup>13</sup> We moderately modified `sbird's SimulationRunner` to generate customized dark matter only simulations using Latin hypercubes.<sup>14</sup>

## DATA AVAILABILITY

The code to reproduce a 50 LR-3 HR emulator is available at [https://github.com/jibanCat/matter\\_multi\\_fidelity\\_emu](https://github.com/jibanCat/matter_multi_fidelity_emu) alongside the power spectrum data.

## ACKNOWLEDGEMENTS

We thank Martin Fernandez, Phoebe Upton Sanderbeck, Mahdi Qezlou, and Shan-Chang Lin for valuable help and discussions on this project. We thank Cosmology from Home 2020 for providing a valuable place for discussing simulation-based inference during the pandemic. SB was supported by NSF grant AST-1817256. Computing resources were provided by NSF XSEDE allocation AST180058.

## REFERENCES

- Abbott T. M. C., et al., 2020, Phys. Rev. D, 102, 023509 (arXiv:2002.11124)
- Agarwal S., Abdalla F. B., Feldman H. A., Lahav O., Thomas S. A., 2014, MNRAS, 439, 2102 (arXiv:1312.2101)
- Amendola L., et al., 2018, Living Reviews in Relativity, 21, 2 (arXiv:1606.00180)
- Barnes J., Hut P., 1986, Nature, 324, 446
- Bird S., Rogers K. K., Peiris H. V., Verde L., Font-Ribera A., Pontzen A., 2019, J. Cosmology Astropart. Phys., 2019, 050 (arXiv:1812.04654)
- Bocquet S., Heitmann K., Habib S., Lawrence E., Uram T., Frontiere N., Pope A., Finkel H., 2020, arXiv e-prints, p. arXiv:2003.12116 (arXiv:2003.12116)
- Bonilla E. V., Chai K., Williams C., 2008. NIPS, <https://proceedings.neurips.cc/paper/2007/file/66368270ffd51418ec58bd793f2d9b1b-Paper.pdf>

trained with 4233 (magneto-)hydrodynamical simulations in a relatively small box,  $25 \text{Mpc}/h$ .

<sup>12</sup> <https://github.com/EmuKit/emukit>

<sup>13</sup> <https://github.com/MP-Gadget/MP-Gadget>

<sup>14</sup> <https://github.com/sbird/SimulationRunner>

<sup>11</sup> Villaescusa-Navarro et al. (2020) has a neural net emulator

- Caldwell R. R., Kamionkowski M., 2009, *Annual Review of Nuclear and Particle Science*, 59, 397 (arXiv:0903.0866)
- Chartier N., Wandelt B., Akrami Y., Villaescusa-Navarro F., 2020, arXiv e-prints, p. arXiv:2009.08970 (arXiv:2009.08970)
- Couchman H. M. P., Thomas P. A., Pearce F. R., 1995, *ApJ*, 452, 797 (arXiv:astro-ph/9409058)
- Cutajar K., Pullin M., Damianou A., Lawrence N., González J., 2019, arXiv e-prints, p. arXiv:1903.07320 (arXiv:1903.07320)
- DESI Collaboration et al., 2016, arXiv e-prints, p. arXiv:1611.00036 (arXiv:1611.00036)
- Damianou A., Lawrence N., 2013, in Carvalho C. M., Ravikumar P., eds, *Proceedings of Machine Learning Research Vol. 31, Proceedings of the Sixteenth International Conference on Artificial Intelligence and Statistics*. PMLR, Scottsdale, Arizona, USA, pp 207–215, <http://proceedings.mlr.press/v31/damianou13a.html>
- Davies C. T., Cautun M., Giblin B., Li B., Harnois-Déraps J., Cai Y.-C., 2020, arXiv e-prints, p. arXiv:2010.11954 (arXiv:2010.11954)
- Dehnen W., 2002, *Journal of Computational Physics*, 179, 27 (arXiv:astro-ph/0202512)
- Euclid Collaboration et al., 2020, arXiv e-prints, p. arXiv:2010.11288 (arXiv:2010.11288)
- Feng J. L., 2010, *ARA&A*, 48, 495 (arXiv:1003.0904)
- Feng Y., Bird S., Anderson L., Font-Ribera A., Pedersen C., 2018a, *MP-Gadget/MP-Gadget: A tag for getting a DOI*, doi:10.5281/zenodo.1451799, <https://doi.org/10.5281/zenodo.1451799>
- Feng Y., Bird S., Anderson L., Font-Ribera A., Pedersen C., 2018b, *MP-Gadget/MP-Gadget: A tag for getting a DOI*, doi:10.5281/zenodo.1451799, <https://doi.org/10.5281/zenodo.1451799>
- Forrester A. I., Söbester A., Keane A. J., 2007, *Proc. R. Soc. A*, 463, 3251–3269
- Frazier P. I., 2018, arXiv e-prints, p. arXiv:1807.02811 (arXiv:1807.02811)
- Giblin B., Cataneo M., Moews B., Heymans C., 2019, *MNRAS*, 490, 4826 (arXiv:1906.02742)
- Greengard L., Rokhlin V., 1987, *Journal of Computational Physics*, 73, 325
- Habib S., Heitmann K., Higdon D., Nakhleh C., Williams B., 2007, *Phys. Rev. D*, 76, 083503 (arXiv:astro-ph/0702348)
- Harnois-Déraps J., Giblin B., Joachimi B., 2019, *A&A*, 631, A160 (arXiv:1905.06454)
- Heitmann K., Higdon D., Nakhleh C., Habib S., 2006, *ApJ*, 646, L1 (arXiv:astro-ph/0606154)
- Heitmann K., Higdon D., White M., Habib S., Williams B. J., Lawrence E., Wagner C., 2009, *ApJ*, 705, 156 (arXiv:0902.0429)
- Heitmann K., Lawrence E., Kwan J., Habib S., Higdon D., 2014, *ApJ*, 780, 111 (arXiv:1304.7849)
- Heitmann K., et al., 2016, *ApJ*, 820, 108 (arXiv:1508.02654)
- Hockney R. W., Eastwood J. W., 1988, *Computer simulation using particles*
- Huang D., Allen T. T., Notz W. I., Miller R. A., 2006, *Struct. Multidisc. Optim.*, 32, 369
- Kennedy M., O'Hagan A., 2000, *Biometrika*, 87, 1 (<https://academic.oup.com/biomet/article-pdf/87/1/1/590577/870001.pdf>)
- Kern N. S., Liu A., Parsons A. R., Mesinger A., Greig B., 2017, *ApJ*, 848, 23 (arXiv:1705.04688)
- Kodi Ramanah D., Charnock T., Villaescusa-Navarro F., Wandelt B. D., 2020, *MNRAS*, 495, 4227 (arXiv:2001.05519)
- Kwan J., Bhattacharya S., Heitmann K., Habib S., 2013, *ApJ*, 768, 123 (arXiv:1210.1576)
- Kwan J., Heitmann K., Habib S., Padmanabhan N., Lawrence E., Finkel H., Frontiere N., Pope A., 2015, *ApJ*, 810, 35 (arXiv:1311.6444)
- Lam R., Allaire D., Willcox K. E., 2015, 56th AIAA/ASCE/AHS/ASC Structures, Structural Dynamics, and Materials Conference
- Lawrence E., Heitmann K., White M., Higdon D., Wagner C., Habib S., Williams B., 2010, *ApJ*, 713, 1322 (arXiv:0912.4490)
- Lawrence E., et al., 2017, *ApJ*, 847, 50 (arXiv:1705.03388)
- Lesgourgues J., 2011, arXiv e-prints, p. arXiv:1104.2932 (arXiv:1104.2932)
- Li Y., Ni Y., Croft R. A. C., Di Matteo T., Bird S., Feng Y., 2020, arXiv e-prints, p. arXiv:2010.06608 (arXiv:2010.06608)
- Liu J., Petri A., Haiman Z., Hui L., Kratochvil J. M., May M., 2015, *Phys. Rev. D*, 91, 063507 (arXiv:1412.0757)
- Lukić Z., Stark C. W., Nugent P., White M., Meiksin A. A., Almgren A., 2015, *MNRAS*, 446, 3697 (arXiv:1406.6361)
- McClintock T., et al., 2019, arXiv e-prints, p. arXiv:1907.13167 (arXiv:1907.13167)
- McLeod M., Osborne M. A., Roberts S. J., 2017, arXiv e-prints, p. arXiv:1703.04335 (arXiv:1703.04335)
- Paley A., Pullin M., Mahsereci M., Lawrence N., González J., 2019, in *Second Workshop on Machine Learning and the Physical Sciences*, NIPS.
- Pedersen C., Font-Ribera A., Rogers K. K., McDonald P., Peiris H. V., Pontzen A., Slosar A., 2020, arXiv e-prints, p. arXiv:2011.15127 (arXiv:2011.15127)
- Peherstorfer B., Willcox K., Gunzburger M., 2018, *SIAM Review*, 60, 550 (<https://doi.org/10.1137/16M1082469>)
- Pellejero-Ibañez M., Angulo R. E., Aricó G., Zennaro M., Contreras S., Stücker J., 2020, *MNRAS*, 499, 5257 (arXiv:1912.08806)
- Perdikaris P., Raissi M., Damianou A., Lawrence N. D., Karniadakis G. E., 2017, *Proc. R. Soc. A*, 473
- Poloczek M., Wang J., Frazier P. I., 2016, arXiv e-prints, p. arXiv:1603.00389 (arXiv:1603.00389)
- Ramachandra N., Valogiannis G., Ishak M., Heitmann K., 2020, arXiv e-prints, p. arXiv:2010.00596 (arXiv:2010.00596)
- Rasmussen C. E., Williams C. K. I., 2005, *Gaussian Processes for Machine Learning (Adaptive Computation and Machine Learning)*. The MIT Press
- Richardson L. F., 1911, *Philosophical Transactions of the Royal Society of London Series A*, 210, 307
- Rogers K. K., Peiris H. V., Pontzen A., Bird S., Verde L., Font-Ribera A., 2019, *J. Cosmology Astropart. Phys.*, 2019, 031 (arXiv:1812.04631)
- Schneider A., et al., 2016, *J. Cosmology Astropart. Phys.*, 2016, 047 (arXiv:1503.05920)
- Spergel D., et al., 2013, arXiv e-prints, p. arXiv:1305.5422 (arXiv:1305.5422)
- Springel V., Hernquist L., 2003, *MNRAS*, 339, 289 (arXiv:astro-ph/0206393)
- Takhtaganov T., Lukic Z., Mueller J., Morozov D., 2019, arXiv e-prints, p. arXiv:1905.07410 (arXiv:1905.07410)
- Tyson J. A., 2002, in Tyson J. A., Wolff S., eds, *Society of Photo-Optical Instrumentation Engineers (SPIE) Conference Series Vol. 4836, Survey and Other Telescope Technologies and Discoveries*. pp 10–20 (arXiv:astro-ph/0302102), doi:10.1117/12.456772
- Villaescusa-Navarro F., et al., 2020, arXiv e-prints, p. arXiv:2010.00619 (arXiv:2010.00619)
- White S. D. M., 1994, arXiv e-prints, pp astro-ph/9410043 (arXiv:astro-ph/9410043)
- White M., 2004, *Astroparticle Physics*, 22, 211 (arXiv:astro-ph/0405593)
- Wong Y. Y. Y., 2011, *Annual Review of Nuclear and Particle Science*, 61, 69 (arXiv:1111.1436)
- Zel'Dovich Y. B., 1970, *A&A*, 500, 13
- Zhai Z., et al., 2019, *ApJ*, 874, 95 (arXiv:1804.05867)
- van Daalen M. P., Schaye J., Booth C. M., Dalla Vecchia C., 2011,



